

Growth and Self-assembly of Nanostructured $\text{CoC}_2\text{O}_4 \cdot 2\text{H}_2\text{O}$ Particles

Ollivier Pujol,^{*,†} Paul Bowen,[‡] Pierre A. Stadelmann,[†] and Heinrich Hofmann[‡]

Interdisciplinary Centre for Electron Microscopy, Swiss Federal Institute of Technology-Lausanne, Building MXC, CH-1015 Lausanne, Switzerland, and Powder Technology Laboratory, Materials Institute, Swiss Federal Institute of Technology-Lausanne, Building MXD, CH-1015 Lausanne, Switzerland

Received: November 19, 2003; In Final Form: May 12, 2004

The growth of $\text{CoC}_2\text{O}_4 \cdot 2\text{H}_2\text{O}$ particles during aqueous precipitation has been followed by several electron microscopy techniques. A multiple-stage growth leading to final particles with a core–shell structure has been observed. In the first stage, the primary particles grow and aggregate to form secondary particles which in turn agglomerate to form the elongated core of the final particles. The final particle crystal faces are formed around the core, layer by layer and face by face, by primary particle self-assembly. The core is disordered and composed of both isolated partially crystalline primary particles and aggregated primary particles. The shell faces are ordered and made up by assembly of strings of 5–7 nm crystalline nanodomains.

Introduction

The manufacture of tailored nanostructured materials with sizes, morphologies, functionalities, and thus controlled properties is currently a great challenge in material science. Precipitation from homogeneous solution is one of several ways to synthesize nanostructured materials. The precipitation of mesoscale particles occurs in several steps. Initially, reactants are mixed to yield a supersaturated solution leading to nucleation. The formed nuclei grow by diffusive processes and become primary particles (PP). Subsequent growth may occur by two different mechanisms: crystal growth and aggregation. Growth processes involve growth by a diffusional mechanism of atomistic or molecular scale units. Ripening processes where larger crystals grow at the expense of smaller ones, minimizing the solid–liquid interfacial surface, may also contribute to crystal growth. Growth by aggregation produces particle assemblies, called secondary particles (SP), built from primary particles which can be ordered or disordered. Some authors have shown the existence of structural building blocks, made up of hundreds or even thousands of atoms, in polycrystalline precipitates.^{1–11} Most polycrystalline particles consist of randomly oriented PP while a few polycrystalline particles or colloidal crystals are made up of highly oriented self-assembled subunits.^{5–11} Precipitates showing such organization are $(\text{NH}_4)_3\text{PW}_{12}\text{O}_{40}$,⁷ $\alpha\text{-Fe}_2\text{O}_3$,⁵ $\text{CuC}_2\text{O}_4 \cdot 0.33\text{H}_2\text{O}$,⁶ BaCrO_4 ,¹⁰ and BaSO_4 .¹¹ The precipitation often occurs in the presence of additives which seem to have a major contribution to self-assembly processes.

Various types of materials are known to self-assemble such as colloidal particles,^{12,13} nanocrystallites,^{14–19} or mesoscale objects^{20,21} which form two-^{14,20} or three-dimensional^{15–19,21} arrays. In these systems, the driving forces to self-assemble are often hydrophobic/hydrophilic interactions. Crystal growth by aggregation is explained by complex formation mechanisms^{16,17,22–31} which are not often understood in detail. According to Matijevic and co-workers,^{22–24} the SP formation is controlled by diffusion and facilitated by changes in the

chemical conditions in the system. This process, similar to addition–polymerization, consists of an irreversible capture of single PP by the growing aggregates. According to the micro-mechanical model developed by Hounslow and co-workers,^{25–28} the PP aggregation process is governed by the collision rate and efficiency, between particles during the suspension stirring. Particles colliding in lower ionic strength solutions may re-align themselves into a more favorable energy state before being fixed into place.²⁷ Penn and Banfield have shown^{8,9,16,17} that some natural minerals grow through such a mechanism of oriented attachment of nanocrystals. The oriented attachment consists of a spontaneous self-organization of adjacent building blocks, sharing a common crystallographic orientation. Then the particles join at a planar interface, reducing the overall energy by removing the contribution associated with unsatisfied bonds. Recently, Jongen et al. discovered a nanometric substructure in copper oxalate precipitates.⁶ The size and morphology of these copper oxalate particles can be controlled by the use of additives. Moreover, the particles retain their morphology and nanometric substructure during decomposition into copper oxide³² and subsequent reduction into the metal. That work led us to study the structure of cobalt oxalate particles precipitated from aqueous solutions to see if a similar nanostructure exists for this material of inherent interest for magnetic applications. The growth mechanism and substructure of such particles are often difficult to determine by techniques like small-angle X-ray scattering^{1,2} or UV–visible spectroscopy³ due to the rapid kinetics or low solid fractions (<0.005). Usually only the morphology and structure of the final particles are observed by electron microscopy.^{5,14,15} As a consequence, the growth of the precipitates has been rarely followed by electron microscopy.⁴ The freezing/sublimation technique used in our work presents the advantage of probing the state of suspension during the precipitation process. The information obtained by low-voltage high-resolution scanning electron microscopy (LVHRSEM) includes the size, the morphology, and the organization of the precipitates during the formation process. The analysis of the precipitates by transmission electron microscopy (TEM) gives the chemical composition, phase, structure, and orientation of the solid at different stages of growth. Other sample preparation

* Corresponding author. E-mail: ollivier.Pujol@epfl.ch. Fax: 0041 21 693 4401.

[†] Interdisciplinary Centre for Electron Microscopy.

[‡] Powder Technology Laboratory, Materials Institute.

techniques, like controlled dissolution, ultramicrotomy, or thinning by ion milling, have also been performed to probe, by electron microscopy, the structural organization of the final precipitate. These techniques have allowed us to build up a detailed but complex picture of the cobalt oxalate particle structure. The particles have a core-shell structure, both of which are nanostructured but with a poorly ordered core and a well-structured shell. A possible mechanism explaining this complex organization is proposed.

Experimental Section

Synthesis. Cobalt oxalate dihydrate (COD) precipitates were synthesized, in aqueous solution at room temperature, by mixing and constant stirring of cobalt nitrate and sodium oxalate solutions. These solutions were prepared from the analytical-grade powders of cobalt(II) nitrate hexahydrate and sodium oxalate (Merck/Darmstadt/Germany) and diluted with ultrapure and filtered water. The cobalt concentration in solution was measured by atomic emission spectroscopy (ICP-AES, Perkin Elmer). The sodium oxalate solution was taken as a primary standard. The precipitation reactions were monitored at room temperature by mixing, at t_0 , 5 mL of 5.2×10^{-3} mol/L cobalt nitrate solution and 5 mL of 5.0×10^{-3} mol/L sodium oxalate solution. The value of the supersaturation was of the order of $S_0 = \log(P_s/K_s) = 3.37$ where P_s is the solubility product and K_s is the solubility constant at 20 °C. The solution was mixed during the whole reaction using a magnetic stirrer at 300 rpm. After 1 h of aging, the suspension was filtered on a 0.2- μm cellulose membrane and the powder was dried 48 h in a desiccator using Silica gel.

Freezing/Sublimation Preparation. The COD particle growth was followed by low-voltage high-resolution scanning electron microscopy (LVHRSEM) using a freezing/sublimation method. Ten microliters of solutions sampled after t minutes of reaction was put on a copper cryo-SEM sample holder in a circular hole (6-mm diameter and 0.2-mm deep). The drop was then pressed with a copper plate to remove the solution in excess. For transmission electron microscopy (TEM) preparation, 10 μL of solution was deposited on a TEM grid (copper grid of 3.05 mm of diameter with amorphous carbon film containing holes) and then put into the cryo-SEM sample holder. The set was plunged into liquid nitrogen (LN_2); the freezing occurred under a vacuum of 4×10^{-4} mbar. After freezing, the sample was transferred to a Gatan Alto 2500 (Gatan/Pleasanton/USA) cryo-chamber mounted on a Philips XL30-FEG Sirion (FEI/Eindhoven/Netherlands) SEM. The aqueous phase sublimation was performed at -80 °C under a vacuum of 5×10^{-6} mbar. After sublimation, the sample was heated to room temperature. A gold layer (mean thickness = 10.0 ± 3.0 nm) was deposited, for the SEM observations, by cathodic sputtering performed on a BioRad E5400 sputter coater (BioRad/Hercules/USA) operating at $P = 10^{-2}$ mbar, $I = 100$ mA, $U = 1$ kV, $t = 30$ s. Other SEM samples were coated by carbon or by Au/Pd particles to ensure the validity of the measurements made on the gold-coated COD particles. The amorphous carbon coating (mean thickness of 25 nm) was performed in a carbon evaporation coater operating at $P = 5.2 \times 10^{-6}$ mbar, $I = 90$ mA, $U = 2.4$ kV, and $t = 10$ s. Au/Pd deposition (particle mean size: 3.3 ± 0.4 nm) was done in the Gatan Alto 2500 cryo-chamber after the aqueous phase sublimation at $P = 2 \times 10^{-3}$ mbar, $I = 8$ mA, $U = 7$ kV, $t = 30$ s, and $T = -150$ °C.

Dissolution. COD (4.8 mg) (obtained after 1 h of reaction) was dissolved in 100 mL of ultrapure and ultrafiltered water at 20 °C for 24 h. Constant magnetic stirring of 300 rpm was

maintained during the reaction. After 24 h, the suspension was filtered on 0.2- μm cellulose membrane, and the powder was dried and weighed. The final powder mass was 2.5 mg. The COD was then dispersed in 2-propanol p.a. in an ultrasonic device for 5 min to prepare SEM and TEM samples.

(101) Final Particle Cross Section by Ultramicrotomy. Dry COD powder obtained after 1 h of reaction was embedded in epoxy resin composed of Agar 100, dodecenyl succinic anhydride (DDSA), methyl nadic anhydride (MNA), and 2,4,6-tri-(dimethylaminomethyl)phenol (DMP30). The mixture of resin and powder was put in a drier at 60 °C for 12 h to allow the polymerization. Then, the block was cut in a dry environment at room temperature with a 35° Diatom diamond knife (radius of 5 nm) mounted on a Reichert-Jung Ultracut E ultramicrotome. The thickness of the cross sections was around 80 nm.

Ion Milling Preparation. A Precision Ion Polishing System (PIPS) 691 Gatan equipped with two guns was used. An epoxy film containing the powder, with a thickness of 270 μm , was stuck on a TEM ring. The sample was then thinned by Ar^+ milling at 4.5 kV at room temperature in total rotation mode for 5 h and 40 min. The incidence angles of the upper and lower beams were respectively fixed to 10° and 6°.

Structural Characterization. A Philips Sirion XL-30 FEG SEM, operated between 0.5 and 30 kV, equipped with a cryo-stage, a field emission gun, and a Trough Lens detector, was used to perform the topographic imagery. The particle structures were studied on a Philips EM-430 TEM operating at 300 kV and equipped with a simple-tilt Gatan cryo sample holder. The chemical analysis was performed with an analytical TEM Hitachi HF-2000 FEG operating at 200 kV (Hitachi High Technologies, Japan), equipped with Dark-STEM and EELS detectors. The X-ray diffractograms were measured using a Siemens D500 diffractometer equipped with a copper anode and a graphite secondary monochromator (Siemens/Berlin/Germany). The measurements were made within a θ range from 5° to 30° with steps of 0.04° and measuring time of 4 s/step.

Results and Discussion

Characterization of Final Particles. The precipitate morphology was characterized after 1 h of reaction by LVHRSEM. The COD precipitates in the form of agglomerated rods between 5 and 40 μm in length. They have an acicular crystalline habit and an organized layered substructure as shown in Figure 1a. The X-ray diffractogram (XRD) of the powder was indexed with a monoclinic structure, space group $P2_1/m$, with unit cell parameters ($a = c = 0.662$ nm, $b = 0.780$ nm, $\beta = 131.57^\circ$) corresponding to γ cobalt oxalate dihydrate³³ as illustrated in Figure 1b. The XRD pattern suggests that the compound contains both crystalline and amorphous material, corresponding to the low angles bump observed between 10° and 30°. The cobalt oxalate dihydrate structure can be described as a polymer-type ribbon as illustrated in Figure 2. The cobalt atom is linked with four oxygen atoms from two oxalate molecules. The C, O, and Co atoms are in the same plane. The ribbons are parallel to the [101] direction. The cobalt atoms and associated water molecules are in the plane of symmetry of the layer. The structure can be viewed as a stacking of identical layers, parallel to (10 $\bar{1}$) plane and translated with respect to each other to produce a succession of planes ABAB.... Each layer is made up of a set of parallel plane ribbons (CoC_2O_4). The crystallites size was calculated with the Scherrer equation,³⁴ from the measurement of the peak broadening for the following reflections ($\bar{1}11$), ($\bar{2}02$), and (040) of the X-ray diffractogram. A standard quartz sample was used to subtract the contribution of

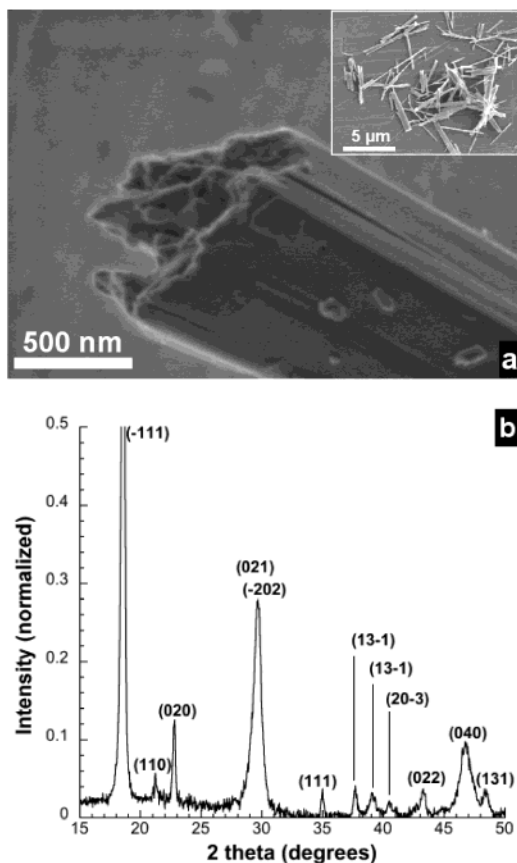


Figure 1. (a) LVHRSEM image of a $\text{CoC}_2\text{O}_4 \cdot 2\text{H}_2\text{O}$ particle aged 1 h in suspension. (b) X-ray diffractogram of a $\text{CoC}_2\text{O}_4 \cdot 2\text{H}_2\text{O}$ powder indexed with a monoclinic structure.³³

the diffractometer to the peak broadening. The mean size of the crystallites is approximately 24 nm in the direction $[\bar{1}11]$, 9 nm along $[\bar{1}01]$, and 10 nm along $[010]$. These values are semiquantitative because of the approximations in the used Scherrer equation³⁵ and the possible contributions from stacking faults to the peak broadening. The atomic force microscopy (AFM) image (Figure 3) shows a nanosized layered structure of both the lateral and basal particle faces; these features seem to be strings of nanodomains oriented along the principal axis of the particle. The step height measured on a basal face is around 5–7 nm.

The COD structure was studied by TEM in diffraction mode at -184°C to minimize irradiation damage. The diffraction patterns obtained were typical of COD single crystals that contain stacking faults along $[010]$ (Figure 4). The electron diffraction pattern corresponding to the $[10\bar{1}]$ zone axis was then simulated by a JEMS program³⁶ for the monoclinic structure.³³ Figure 4b represents a superposition of the experimental and simulated electron diffraction patterns. The simulated structure fits the experimental data well, indicating that the particle faces have been correctly indexed. The $(10\bar{1})$ and (010) correspond to the basal and lateral faces, respectively, as illustrated in Figure 4c. In conclusion, the final particle seems to be a polycrystal made up by strings of nanodomains oriented along the $[10\bar{1}]$ direction and arranged in layers. The lateral and basal faces of the precipitate are composed of stacked layers, with the layer thickness varying between 5 and 7 nm. The precipitate substructure will be investigated in the next section at different times of reaction to understand the growth mechanism and the internal organization of the particle.

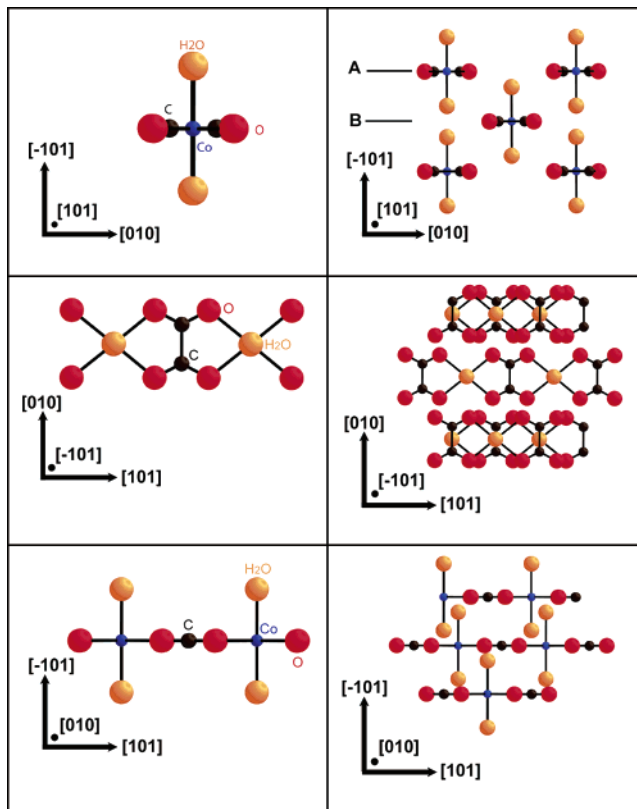


Figure 2. Orientation and ribbon arrangement in $\text{CoC}_2\text{O}_4 \cdot 2\text{H}_2\text{O}$ γ phase structure.³³

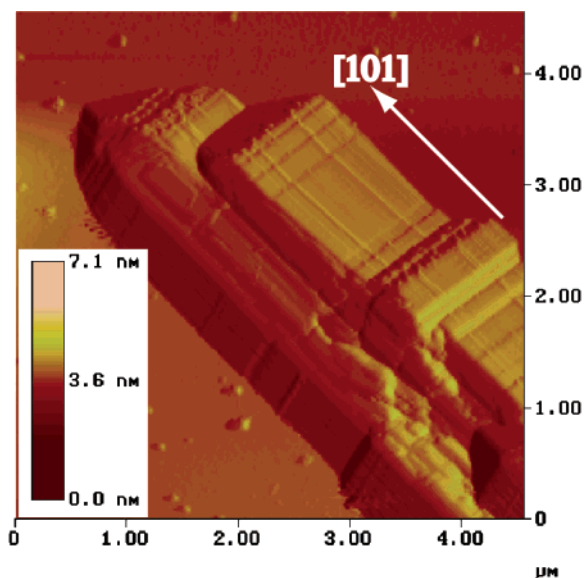


Figure 3. AFM image of a $\text{CoC}_2\text{O}_4 \cdot 2\text{H}_2\text{O}$ particle aged 1 h in suspension.

Particles Growth Followed by LVHRSEM Using a Freezing/Sublimation Technique. Figure 5 presents LVHRSEM micrographs recorded after five different freezing times and using different conductive coatings. After 4 min of reaction, one can observe clusters of nanoparticles on the sample holder surface, as illustrated in Figure 5a. These clusters are assumed to have formed during sample preparation from the two types of particles observed: spherical particles marked A and more elongated particles marked B which are freely dispersed before drying on the sample holder. The third type of 10-nm-sized nanoparticles marked C comes probably from the gold coating

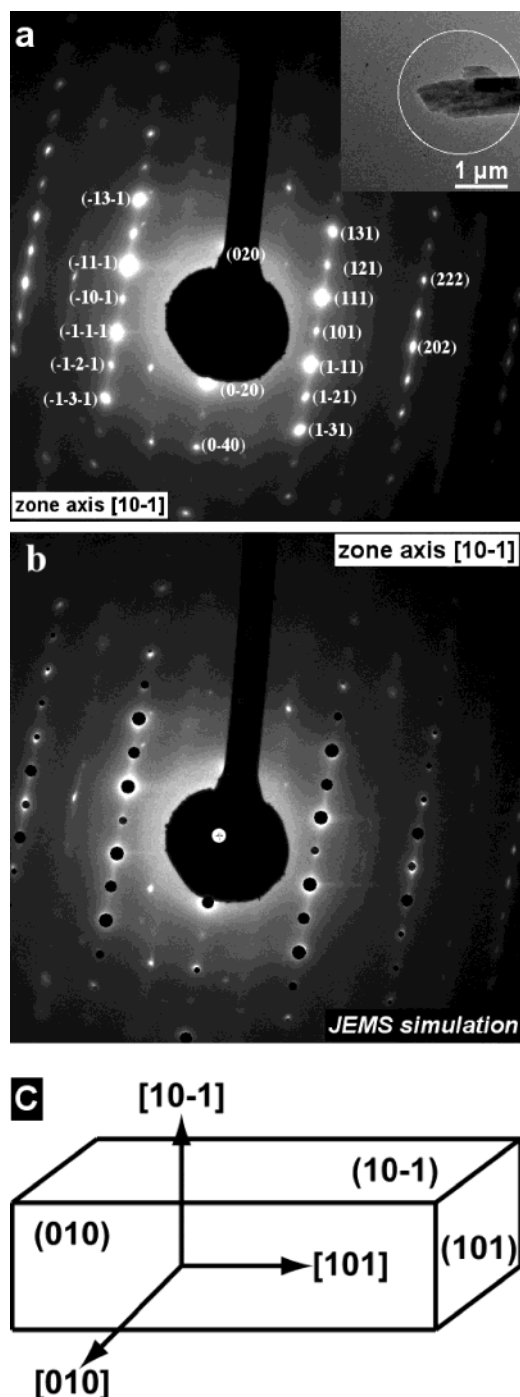


Figure 4. (a) SAEDP at $-184\text{ }^{\circ}\text{C}$, indexed with a monoclinic structure,³³ of a final particle aged 1 h in suspension. (b) $[10\bar{1}]$ EDP simulation (dark dots) by JEMS of the theoretical $\text{CoC}_2\text{O}_4 \cdot 2\text{H}_2\text{O}$ monoclinic structure.³³ (c) Orientation of $\text{CoC}_2\text{O}_4 \cdot 2\text{H}_2\text{O}$ crystal habit with monoclinic structure.³³

(lower insert in Figure 5f). The nanoparticles A, called secondary particles (SP), are nearly spherical and have a mean size of $23 \pm 2\text{ nm}$. The crystallite size, measured from XRD peak broadening of the final particles, suggests that primary particles are smaller than those, marked A, observed after 4 min by LVHRSEM, at least in two of three directions analyzed. The elongated nanoparticles B, called cores of final particles, seem to be aggregates of the secondary particles. After 6 min of reaction (Figure 5b), one observes the growth of elongated particles on an uncoated sample. Their size varies between 50 and $325 \pm 9\text{ nm}$. It was observed that the measured size was

always a multiple of 25 nm, suggesting a growth by attachment of the 25-nm secondary particles. The presence of isolated 25-nm-sized secondary particles on the sample holder supports this assumption. One can observe too the presence of isolated $10 \pm 3\text{ nm}$ sized nanoparticles on the surface of the uncoated sample holder. These particles correspond to primary particles (PP).

After 8 min of reaction, one can observe two structural features (Figure 5c) that may help us understand the final particle formation mechanism. First, one can see the agglomeration of polydispersed nanoparticles (mean size of $23 \pm 4\text{ nm}$) occurring at the end and center of the growing particle. The mean size of these building blocks is the same as that observed for the secondary particles after 4 and 6 min of reaction. In addition, there is a layer by layer growth on the lateral external faces. These show growth fronts on each face with a set of steps and kinks (arrow in Figure 5c). The mean step height measured on each face is $10 \pm 4\text{ nm}$ that could correspond to the gold coating. After 15 min of reaction (Figure 5d), we can begin to recognize the final particle with its layered substructure and its nanograin surface string features. The mean size of nanoparticles at the surface is $10 \pm 3\text{ nm}$ corresponding to the mean steps height (Sh arrow in Figure 5d) and to the mean layers thickness (Lt arrow). The kink size (Ks arrow) measured on Figure 5d is a multiple of 10 nm. After 15 min of reaction, we observe on the sample holder surface some isolated $8 \pm 3\text{ nm}$ nanoparticles, called primary particles (PP), secondary particles ($24 \pm 3\text{ nm}$), aggregates of secondary particles (core of the final particles), and final particles.

Figure 5f shows the topography of conductive (sample holder) and insulating (glass) flat surfaces after a gold coating realized in the standard conditions. In the case of the conductive surface, Au nanoparticles have a mean size of $10 \pm 3\text{ nm}$; they are agglomerated and the surface covering is total. In the case of an insulating surface (like COD), the mean Au particles size is $15 \pm 3\text{ nm}$; Au particles are isolated so that the surface covering is lower than that in the conductive case. The nanoparticles feature observed on the COD surface (Figure 5d) could be partially due to the gold particles deposition (presence of nanoparticles smaller than 8 nm). Other measurements of nanoparticle sizes and layer thicknesses have been made with a suspension, frozen after 10 min of reaction. Samples were uncoated or coated with an amorphous carbon layer (thickness of 25 nm) or with Au/Pd nanoparticles (mean diameter of $3.3 \pm 0.4\text{ nm}$) to ensure the validity of the measurements made on the gold-coated COD particles. Figure 5g–i illustrates the topographies of coated and uncoated particles. The secondary particles mean size measured on the (101) face of carbon-coated and uncoated particles is $26 \pm 4\text{ nm}$. The mean step height measurements on Pd/Au-coated final particles give a value of $10 \pm 3\text{ nm}$ and the layers exhibit a mean thickness of $10 \pm 3\text{ nm}$. The layers on the uncoated final particles exhibit a mean thickness of $7 \pm 2\text{ nm}$ and present a 5–7-nm-sized roughness along $[101]$. The $7 \pm 2\text{ nm}$ step height is consistent with the similar measurements made by AFM. The 5–7 nm crystallite sizes are also coherent with the XRD line-broadening sizes for the $[101]$ and $[010]$ directions presented earlier.

The lateral COD faces exhibit terraces, steps, and kinks and are composed by 5–7-nm-sized primary particles (PP) arranged in layers. The $7 \pm 2\text{ nm}$ mean step height along $[101]$ and $[010]$ directions measured by AFM and LVHRSEM is about 10 times bigger than the (101) and (010) interreticular distances. This indicates a PP aggregation process rather than crystalline growth of the faces. The presence of isolated PP on the sample holder after 15 min of reaction (Figure 5e) is in agreement with this

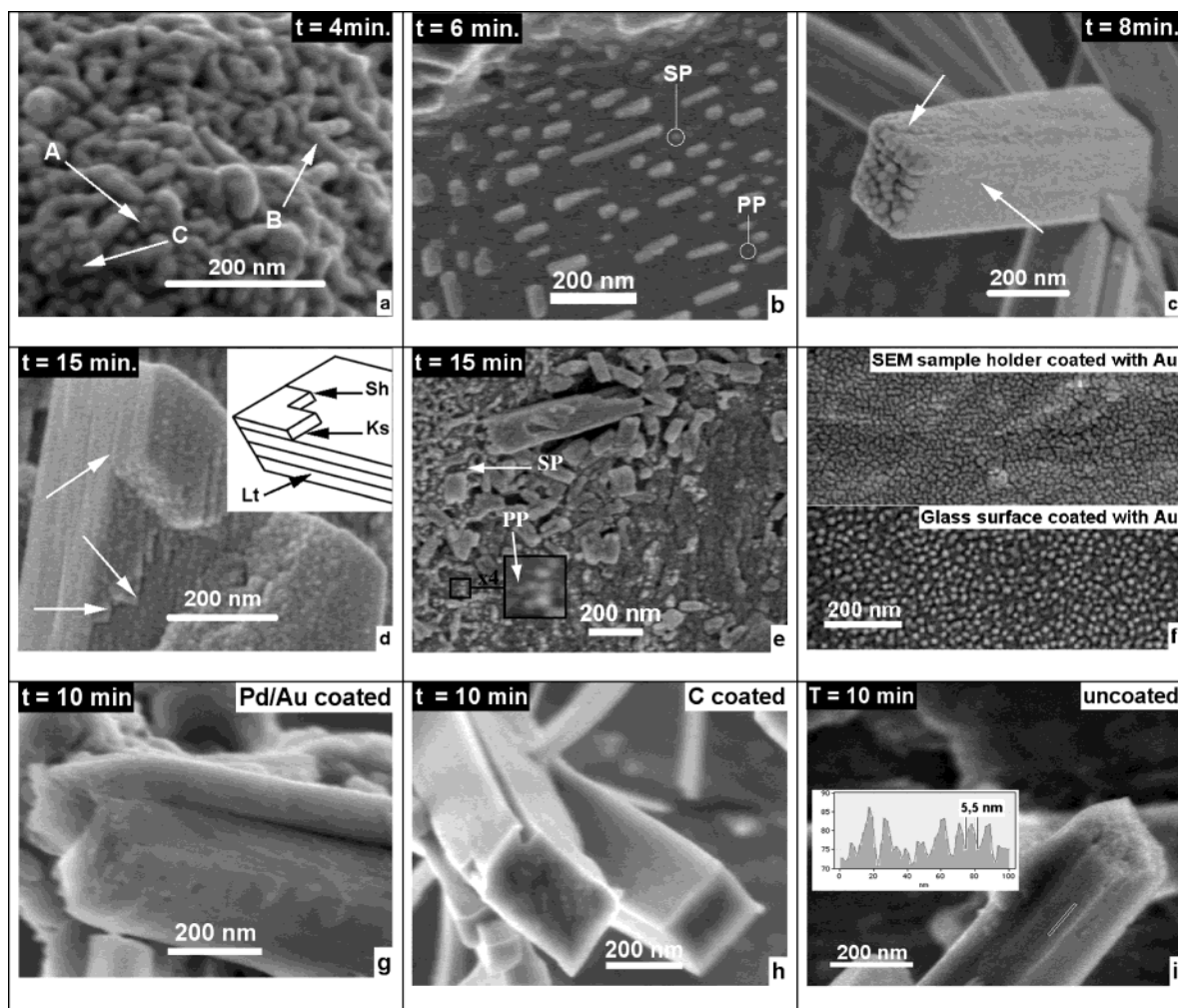


Figure 5. (a) LVHRSEM micrograph of Au-coated cobalt oxalate nanoparticles frozen after 4 min of reaction. The nanoparticles marked A, B, and C correspond respectively to secondary particle, core of final particle, and gold nanoparticle. (b) LVHRSEM micrograph of uncoated cobalt oxalate secondary particles (core) frozen after 6 min of reaction. The primary particles (PP) and secondary particles (SP) are surrounded. (c) LVHRSEM micrograph of Au-coated cobalt oxalate secondary particle frozen after 8 min of reaction. (d) LVHRSEM micrograph of Au-coated cobalt oxalate particle frozen after 15 min of reaction. The step height (Sh), kink size (Ks), and layer thickness (Lt) are indicated by the arrows. (e) LVHRSEM micrograph of Au-coated cobalt oxalate particles frozen after 15 min of reaction. The area surrounded was magnified 4 times to view the primary particles. (f) LVHRSEM micrographs of sample holder (upper insert) and glass surface (lower insert) coated with Au nanoparticles. The micrograph was recorded in the same experimental conditions as d. (g) LVHRSEM micrograph of Pd/Au-coated cobalt oxalate particle frozen after 10 min of reaction. (h) LVHRSEM micrograph of C-coated cobalt oxalate particle frozen after 10 min of reaction. (i) LVHRSEM micrograph of uncoated cobalt oxalate particle frozen after 10 min of reaction. The insert corresponds to an intensity profile taken on a lateral face along a layer.

assumption. So the facet's growth mechanism seems to be an ordered self-assembly of primary particles into the stringlike features initially observed on the final particles by AFM (Figure 3). From these observations one concludes that the final precipitate is a core/shell particle and that the growth seems to be governed by two different mechanisms. The core is formed by agglomeration of polydispersed secondary particles and the faces are formed, layer by layer, by the self-assembly of 5–7-nm primary particles. The presence of steps and kinks reminds us of the classical models of crystal growth, with the major difference being that here the building blocks are not single atoms or molecules but colloidal nanoparticles.

Characterization of the Precipitate's Core. The chemical analysis of the primary and secondary particles has been performed by electron energy loss spectroscopy (EELS), in scanning transmission electron microscopy (STEM) mode, at $-184\text{ }^{\circ}\text{C}$ on a sample frozen after 8 min of reaction. Figure 6 presents a dark STEM image of an area analyzed by EELS and the insert represents the corresponding EEL spectrum. These two different types of particles both contain C, O, and Co atoms.

The mean atomic ratio Co/O measured from 10 spectra is 0.26 ± 0.047 corresponding to the expected 0.25 for CoC_2O_4 . The electron diffraction pattern, taken at $-184\text{ }^{\circ}\text{C}$ of a primary and secondary particle cluster frozen after 8 min, indicates an amorphous structure. This could explain the amorphous contribution, corresponding to the low-angles bump, measured by X-ray diffraction in Figure 1b in the final particles after 60 min. The TEM bright field image of the frozen sample after 8 min in Figure 7a shows the core growth in progress; the structure is formed by the agglomeration of distinct and disordered secondary particles. Their size varies between 15 and 35 nm. In a higher magnification image of this core presented in Figure 7b, we can see that the building blocks are randomly arranged and do not present a long-range order. In fact, the constituting units seem to be partially crystalline and are less than 8 nm. The secondary particles observed by LVHRSEM after 4 min of reaction seem to be agglomerates of these smaller nanograins or poorly crystalline primary particles. The particle arrangement in the core has also been investigated by TEM, at $-184\text{ }^{\circ}\text{C}$, on [101] cross sections of final particles (60 min), prepared by

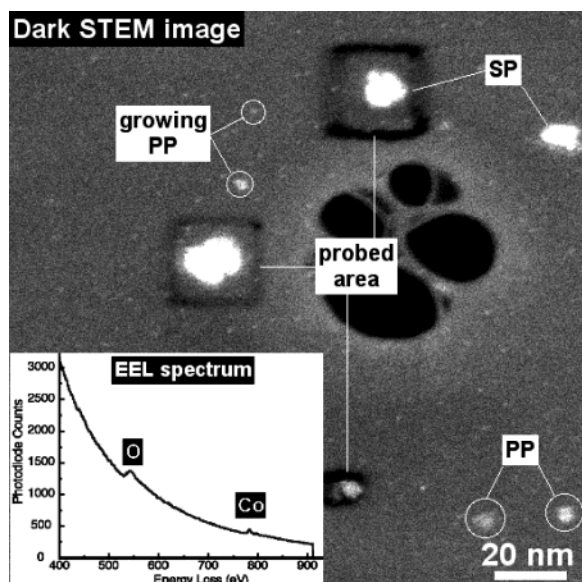


Figure 6. Dark STEM image at $-184\text{ }^{\circ}\text{C}$ of primary particles and secondary particles frozen after 8 min of reaction. The insert presents an EEL spectrum of an analyzed area.

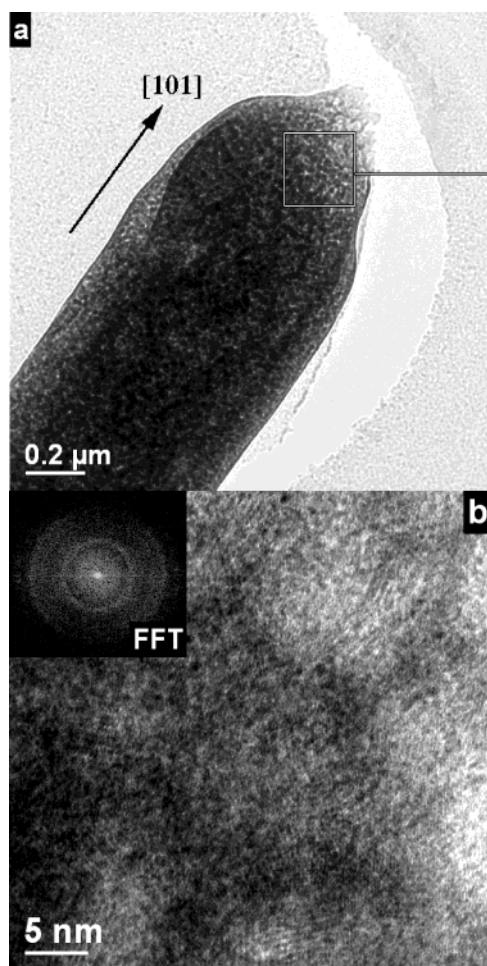


Figure 7. (a) TEM bright field image at $-184\text{ }^{\circ}\text{C}$ of a particle core frozen after 8 min of reaction. (b) Higher magnification TEM image at $-184\text{ }^{\circ}\text{C}$ of the same particle's core and fast Fourier transform (FFT) of the image.

ultramicrotomy. Figure 8 presents a view of the particle as well as bright field and dark field images near an edge. In the main image a hole can be observed in the center of particle. This is

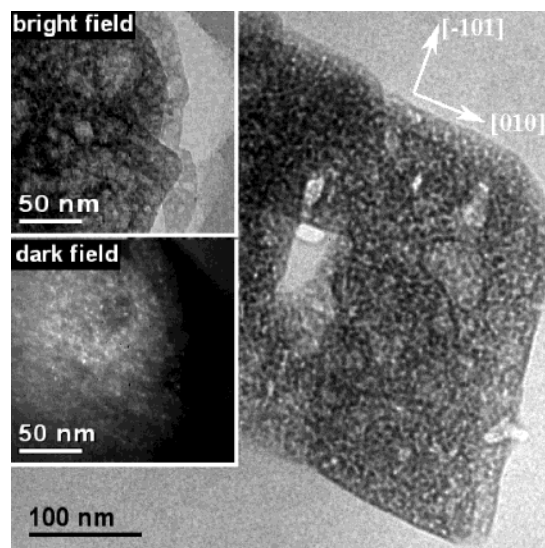


Figure 8. TEM image, at $-184\text{ }^{\circ}\text{C}$, of a (101) cross section of a final COD particle embedded in epoxy resin. The inserts present bright field and dark field images of similar corner of another particle.

probably due to grain pull-out during the microtomy because of a density and porosity difference between the center and the edges of the particle. The (101) face exhibits in bright field a disordered mosaic structure with polydispersed secondary particles. In dark field mode, we notice that the size of the crystalline domains is smaller than 8 nm, coherent with the cryogenic TEM analysis on the sample frozen after 8 min.

Characterization of the Precipitate's Faces. To analyze the structure of the shell faces, the core of the final particles is dissolved as explained in the Experimental Section. The difference in dissolution rates between the core and the shell is probably due to the higher porosity of the core (to its poor order and lower crystallinity too). An LVHRSEM image of a coreless particle is shown as an insert in Figure 9a. A fast structural disorganization of these faces due to e-beam irradiation is observed by TEM at $-184\text{ }^{\circ}\text{C}$ in diffraction mode. After less than 10 s the COD single-crystal diffraction pattern is transformed into a COD powder diffraction pattern, as illustrated in the insert in Figure 9a, and then into diffuse rings characteristic of an amorphous solid. So it seems that the beam induces a random rotation of the crystallites and then the destruction of the long-range order in the structure. Dark field TEM images formed using the closely spaced spots aligned at the (111) and (404) reflections position show rotation moiré fringes, indicating that the faces are crystalline and formed by overlapping crystalline structural units within each face as illustrated in Figure 9b,c. Another type of sample is observed after an ion milling preparation. The COD "single-crystalline" structure, observed in the first few seconds for the particles, is not totally affected by the irradiation. Figure 10a shows the nanostructure of a (101) face. We observe planes of strings of nanograins and a certain alignment of these building blocks following the [101] direction corresponding to growth axis of the cobalt oxalate ribbon. The mean thickness of the strings, measured from intensity profiles on the micrograph, in the [010] direction is on the order of $5 \pm 1\text{ nm}$. The length of the nanograins following the [101] direction is 4–7 nm. The dimensions of these building blocks have the same order of magnitude as the primary particles that make up the secondary particles. A TEM (020) dark field image of the previous area is presented in Figure 10b, illustrating the polycrystalline structure of the precipitate.

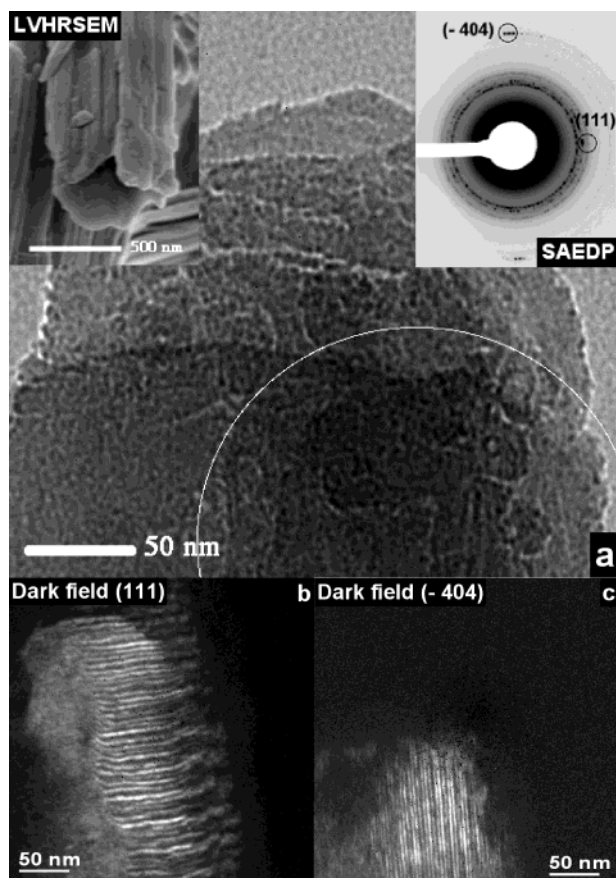


Figure 9. (a) TEM image at $-184\text{ }^{\circ}\text{C}$ with the corresponding EDP of a final particle observed after dissolution and LVHRSEM micrograph of a COD particle observed after dissolution. (b) Corresponding TEM dark field (111) image. (c) Corresponding TEM dark field (-404) image.

The particles features on these TEM images using the ion milling preparation are very similar to those observed with AFM in Figure 3.

Discussion. We have observed by several imaging techniques that cobalt oxalate dihydrate (COD) precipitated from aqueous solution has a complex core-shell structure. This structure seems to be built up in a series of steps leading to the final COD particle. In Figure 11 we have presented a schematic representation of a possible multistep mechanism for the COD precipitate growth. The proposed mechanism takes us progres-

sively from isolated 5–7-nm-sized partially crystalline primary particles (see Figure 7b) to 5–40- μm -long particles with a disordered core and a polycrystalline superstructure shell composed of self-assembled nanograins (see Figures 3 and 4). The different steps of solid formation are linked to the time of reaction, inducing a relationship between the evolution of chemical parameters in the suspension and an increase of the order in the precipitate.

According to the classical theory of precipitation, at high supersaturations a fast nucleation burst occurs when the precursor monomers (atoms or molecules) reach a critical concentration. The nucleation is then followed by the growth of the nucleus to form primary particles. This step occurs just after mixing the reactants and during the first 4 min of reaction. The primary particles have a size around 7 nm and present only a short-range order (as illustrated in Figure 7). During the first minutes of reaction, a high rate of the primary particle growth may explain their partially crystalline structure. Also, the high ionic concentration would lead to a relatively thin electrical double layer, allowing attractive van der Waals forces to dominate any electrical double-layer repulsion. Four minutes after the mixing, we observed clusters of secondary particles and their agglomeration to form the elongated core of the final particle (Figure 5a). The secondary particles, formed by the aggregation of primary particles (Figures 6 and 7), have a disordered and partially crystalline structure (Figure 7) and a mean size of 25 nm. The aggregation of primary particles to form secondary particles can be described with a micro-mechanical model²⁸ of aggregation. But existing models cannot explain the secondary particles agglomeration leading to an anisotropic core. The high polydispersity of core sizes is most likely due to the uncontrolled mixing of reactants (Figure 5b).

After 8 min of reaction, we observed the coexistence of distinct primary particles, secondary particles, and partially formed final particles. In our proposed mechanism the final particle grows by two distinct mechanisms. In the [101] direction, the growth occurs by agglomeration of disordered and polydispersed secondary particles (Figure 5c). On (010) and ($\bar{1}01$) faces, we observe an ordered arrangement of monodispersed primary particles, layer by layer and face by face, leading to the final acicular morphology of the precipitate (Figure 5d). The proposition of a brick by brick growth mechanism for the shell is supported by the fact that the faces are polycrystalline (Figures 3, 5d,e, and 10a,b) composed of strings of monodispersed nanodomains (Figures 3 and 5d,e) like in a colloidal

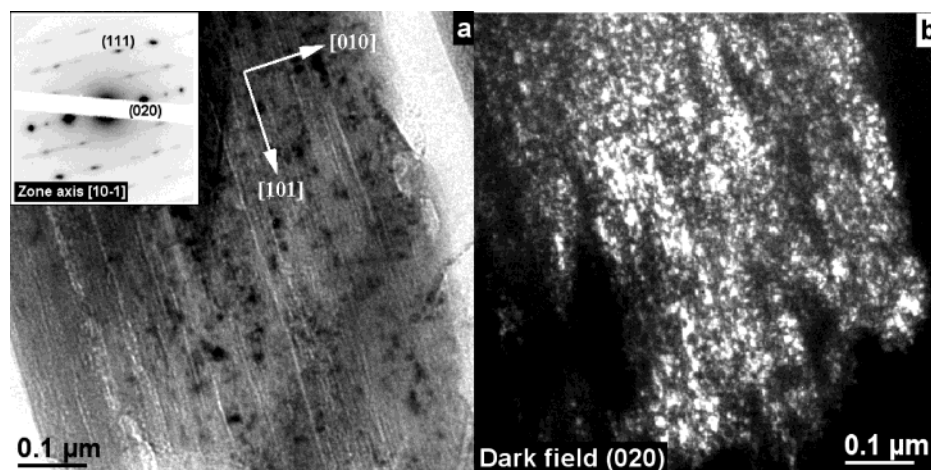


Figure 10. (a) TEM bright field image and SAED, at room temperature, of a $\text{CoC}_2\text{O}_4 \cdot 2\text{H}_2\text{O}$ particle embedded in resin and thinned by Ar^+ ion milling after aging of 1 h. (b) Corresponding (020) TEM dark field image.

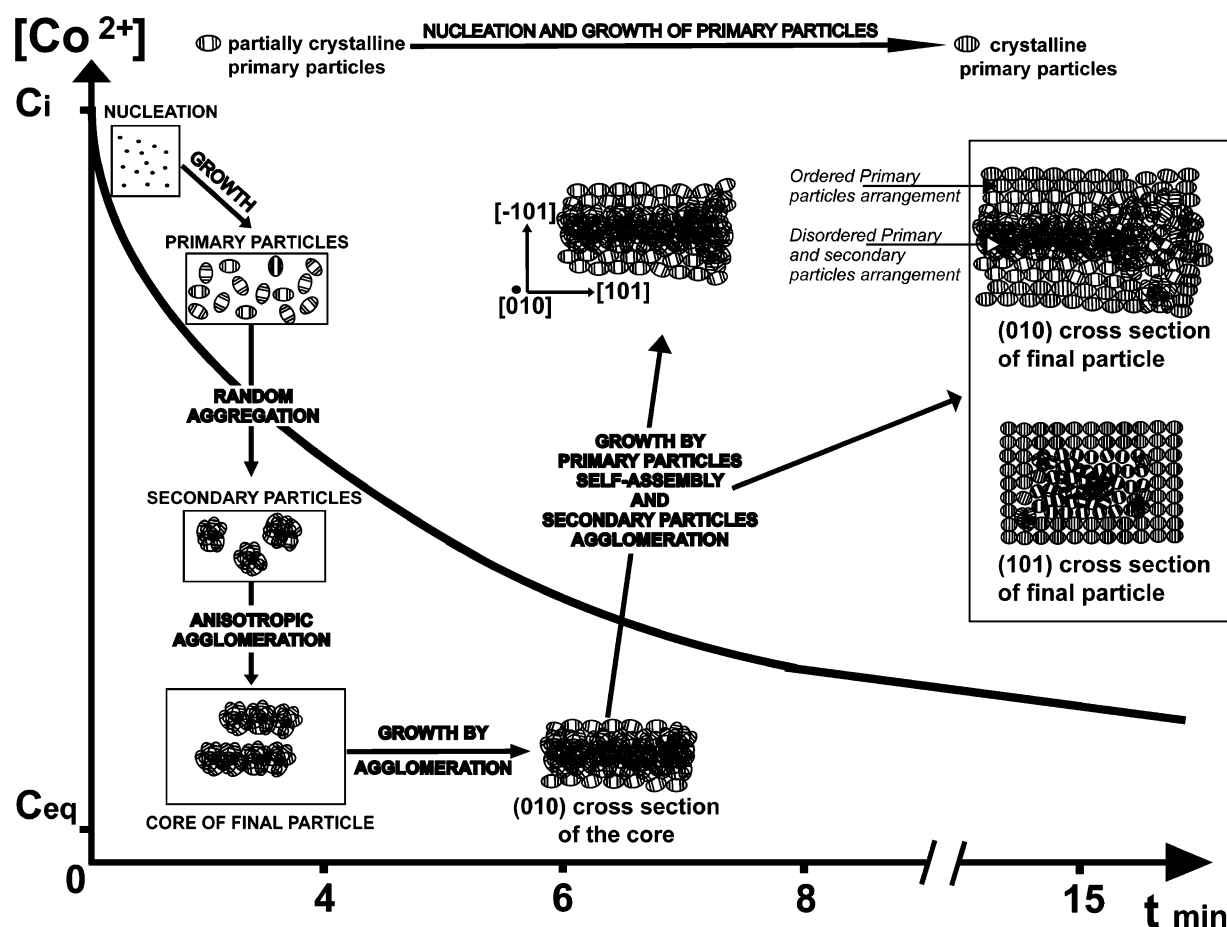


Figure 11. Description of steps and mechanisms of growth leading to final COD particles.

crystal (Figure 4a and insert in Figure 10a). The presence of isolated primary particles on the sample holder after 8 min (Figure 6) and 15 min of reaction (Figure 5e) reinforce this idea. Also, the existence of terraces, steps, kinks, and front of growth on the faces (Figures 3 and 5c–e,g) is not consistent with a surface nucleation mechanism. The final particle presents us with a final core/shell structure, with a partially crystalline core and a polycrystalline shell (Figures 9 and 10).

It seems that the evolution of supersaturation and consequently ionic strength with time play a preponderant rule in nanoparticles ordering. The nanoparticles constituting the shell are crystalline, indicative of a late-developing process of nucleation and a slower growth due to the supersaturation decrease after the initial burst of nucleation and precipitation that formed the partially crystalline core. Furthermore, the observation of isolated crystalline primary particles, after 8 min of reaction, suggests a continuous nucleation process similar to that proposed by Nomura et al.³⁷ The authors demonstrate that new nuclei can be formed in the region where the nuclei or primary particles concentration is so low that the monomer generation rate is larger than the diffusion depletion rate so the monomer concentration increases with time until the critical concentration for nucleation is reached. This process is intensified by the primary particles aggregation into secondary particles that leads to a decrease of their concentration. The self-assembly seems to be followed by a cementation step²⁷ of the primary particles probably caused by the condensation of monomers³⁷ around the contact surface between two building blocks to minimize the surface energy. From a structural point of view, we have noticed that there exists an increase in order in the

[010], $[10\bar{1}]$, and $[101]$ directions from the core toward the faces and the end of particles (Figure 8). This has also been observed recently for nanostructured ZnO particles in the presence of polymeric additives.³⁸ In our proposed mechanism the ordered aggregation step would occur at lower supersaturation than the initial level after mixing, hence a lower ionic strength and lower aggregation rate.^{22–24,27} In these conditions, the primary particles would have a thicker electrical double layer, which may slow the collision, giving more time for the particle to diffuse on the surface and to rotate before being fixed at an energetically favorable site. The alignment could be facilitated by the intrinsic electric fields of primary particles polar crystal lattice^{31,39} or/and by the crystalline anisotropic structure of cobalt oxalate dihydrate molecule, in addition to the oriented attachment.^{8,9,16,17} Also the anisotropic nature of the structure and strong magnetic moment associated with cobalt atom may lead to a magnetic contribution to the anisotropic nature of the core.⁴⁰

In summary, we have followed by several electron microscopy techniques the different stages of the COD particle construction from nanoscale to mesoscale. At first, nucleation and growth occur from the supersaturated solution to give the 5–7-nm-size partially crystalline primary particles. These primary particles then aggregate to form disordered secondary particles. The primary and the secondary particles agglomerate to form the anisotropic core of the final particle. The core acts as a template for the third step of growth which corresponds to the self-assembling and alignment, layer by layer around the core, of crystalline primary particles. The final COD particle has a core/shell structure with a partially crystalline core and a polycrystalline shell. The self-assembly occurs in the last step

of growth where we have a lower ionic strength and supersaturation, inducing slower kinetics of growth and aggregation. Moreover, the crystalline order in the primary and secondary particles increase with the time of reaction, consistent with a continuous process of primary particle nucleation and growth. Population balance modeling should add further weight to these mechanistic propositions. The use of cryogenic electron microscopy (low-voltage high-resolution scanning electron microscopy and transmission electron microscopy) has been shown to be a powerful tool in helping understand the time-dependent aspects of particle growth. The use of such techniques with other systems where the final precipitate appearance may hide particle substructures will help elucidate growth mechanisms and allow finer control of nanostructured materials for many applications.

Acknowledgment. We thank A. Sfera, J. Cagnon, D. Laub, A. Radenovic, L. Soare, and P. Buffat for technical assistance and stimulating discussions. This work is supported by the Swiss National Science Foundation (FN 2100-056643.99/1).

References and Notes

- (1) Tokumoto, M. S.; Pulcinelli, S. H.; Santilli, C. V.; Craievich, A. F. *J. Non-Cryst. Solids* **1999**, *247*, 176–182.
- (2) Meyer, W. R.; Pulcinelli, S. H.; Santilli, C. V.; Craievich, A. F. *J. Non-Cryst. Solids* **2000**, *273*, 41–147.
- (3) Sugimoto, T.; Dirige, G.; Muramatsu, A. *J. Colloid Interface Sci.* **1996**, *182*, 444–456.
- (4) Counter, J.; Addai-Mensah, J.; Ralston, J. *Colloids Surf. A* **1999**, *154*, 389–398.
- (5) Park, G. S.; Shindo, D.; Waseda, Y.; Sugimoto, T. *J. Colloid Interface Sci.* **1996**, *177*, 198–207.
- (6) Jongen, N.; Bowen, P.; Lemaître, J.; Valmalette, J.-C.; Hofmann, H. *J. Colloid Interface Sci.* **2000**, *226*, 189–198.
- (7) Ito, T.; Inumaru, K.; Misono, M. *J. Phys. Chem. B* **1997**, *101*, 9958–9963.
- (8) Penn, R. L.; Banfield, J. F. *Geochim. Cosmochim. Acta* **1999**, *63*, 1549–1557.
- (9) Penn, R. L.; Oskam, G.; Strathmann, T. J.; Searson, P. C.; Stone, A. T.; Veblen, D. R. *J. Phys. Chem. B* **2001**, *105*, 2177–2182.
- (10) Li, M.; Schnablegger, H.; Mann, S. *Nature* **1999**, *402*, 393–395.
- (11) Qi, L.; Cölfen, H.; Antonietti, M. *Chem. Mater.* **2000**, *12*, 2392–2403.
- (12) Velez, O. D.; Lenhoff, A. M.; Kaler, E. W. *Science* **2000**, *287*, 2240–2243.
- (13) Xia, Y.; Gates, B.; Yin, Y.; Lu, Y. *Adv. Mater.* **2000**, *12*, 693–713.
- (14) Yin, J.; Wang, Z. *Phys. Rev. Lett.* **1997**, *79*, 2570–2573.
- (15) Yin, J.; Wang, Z. *J. Mater. Res.* **1999**, *14*, 503–508.
- (16) Penn, R. L.; Banfield, J. F. *Science* **1998**, *281*, 969–971.
- (17) Banfield, J. F. et al. *Science* **2000**, *289*, 751–754.
- (18) Murray, C. B.; Kagan, C. R.; Bawendi, M. G. *Science* **1995**, *270*, 1335–1338.
- (19) Sun, S. et al. *Science* **2000**, *287*, 1989–1992.
- (20) Bowden, N.; Terfort, A.; Carbeck, J.; Whitesides, G. M. *Science* **1997**, *276*, 233–235.
- (21) Oliver, S. R. J.; Bowden, N.; Whitesides, G. M. *J. Colloid Interface Sci.* **1999**, *224*, 425–428.
- (22) Matijevic, E. *Langmuir* **1994**, *10*, 8–16.
- (23) Privman, V.; Goia, D. V.; Park, J.; Matijevic, J. *Colloid Interface Sci.* **1999**, *213*, 36–45.
- (24) Park, J.; Privman, V.; Matijevic, E. *J. Phys. Chem. B* **2001**, *105*, 11630–11635.
- (25) Bramley, A. S.; Hounslow, M. J.; Ryall, R. L. *Chem. Eng. Sci.* **1997**, *52*, 747–757.
- (26) Hounslow, M. J.; Bramley, A. S.; Paterson, W. R. *J. Colloid Interface Sci.* **1998**, *203*, 383–391.
- (27) Collier, A.-P.; Hetherington, C. J. D.; Hounslow, M. J. *J. Cryst. Growth* **2000**, *208*, 513–519.
- (28) Hounslow, M. J.; Mumtaz, H. S.; Collier, A. P.; Barrick, J. P.; Bramley, A. S. *Chem. Eng. Sci.* **2001**, *56*, 2543–2552.
- (29) Sung, M. H.; Choi, I. S.; Kim, J. S.; Kim, W. S. *Chem. Eng. Sci.* **2000**, *55*, 2173–2184.
- (30) Yeadon, M. et al. *Appl. Phys. Lett.* **1998**, *73*, 3208–3210.
- (31) Cölfen, H.; Mann, S. *Angew. Chem., Int. Ed.* **2003**, *42*, 2350–2365.
- (32) Jongen, N.; Hofmann, H.; Bowen, P.; Lemaître, J. *J. Mater. Sci. Lett.* **2000**, *19*, 1073–1075.
- (33) Avond, G.; Pezerat, H.; Lagier, J.; Dubernat, J. *Rev. Chim. Minér.* **1969**, *6*, 1095–1106.
- (34) Scherrer, P. *Nachr. Ges. Wiss. Göttingen* **1918**, 98–100.
- (35) Warren, B. E. *X-ray Diffraction*; Dover: New York, 1990.
- (36) Stadelmann, P. A. *Ultramicroscopy* **1987**, *21*, 131–146.
- (37) Nomura, T. et al. *J. Colloid Interface Sci.* **2000**, *221*, 195–199.
- (38) Taubert, A.; Kübel, C.; Martin, D. C. *J. Phys. Chem. B* **2003**, *107*, 2660–2666.
- (39) Bush, S. et al. *Eur. J. Inorg. Chem.* **1999**, 1643–1653.
- (40) Ocaña, M.; Morales, M. P.; Serna, C. J. *J. Colloid Interface Sci.* **1995**, *171*, 85–91.